Title

From Retinal Waves to Activity-Dependent Retinogeniculate Map Development

Authors and Affiliations

Jeffrey Markowitz[1,2,3], Yongqiang Cao[1,2,3], and Stephen Grossberg[1,2,3*]

[1]Center for Adaptive Systems, Boston University, Boston, MA 02215
[2]Department of Cognitive and Neural Systems, Boston University, Boston, MA 02215
[3]Center of Excellence for Learning in Education, Science and Technology, Boston University, Boston, MA 02215

All correspondence should be addressed to
Professor Stephen Grossberg
Center for Adaptive Systems
Boston University
677 Beacon Street
Boston, MA 02215
Email: steve@bu.edu
Phone: 617-353-7858/7
Fax: 617-353-7755

Abstract

A neural model is described of how spontaneous retinal waves are formed in infant mammals, and how these waves organize activity-dependent development of a topographic map in the lateral geniculate nucleus, with connections from each eye segregated into separate anatomical layers. The model simulates the spontaneous behavior of starburst amacrine cells and retinal ganglion cells during the production of retinal waves during the first few weeks of mammalian postnatal development. It proposes how excitatory and inhibitory mechanisms within individual cells, such as Ca^{2+}-activated K^+ channels, and cAMP currents and signaling cascades, can modulate the spatiotemporal dynamics of waves, notably by controlling the after-hyperpolarization currents of starburst amacrine cells. Given the critical role of the geniculate map in the development of visual cortex, these results provide a foundation for analyzing the temporal dynamics whereby the visual cortex itself develops.

Author Summary

The development of the visual system includes the formation of topographic maps. These maps organize light falling on the retinas of both eyes into brain representations of the 3D world. During the first few weeks of mammalian postnatal life, spontaneous waves of activity occur in both retinas that help to organize the formation of a topographic map from both eyes to the lateral geniculate nucleus, with connections from each eye terminating in a different layer of the geniculate. We model how these waves form and how they can organize the development of the

42 geniculate map. Because the lateral geniculate is the source of all inputs to the visual cortex,
43 these results provide a foundation for better understanding how the visual cortex itself develops.
44

Running Head

46 Retinal waves and retinogeniculate map development
47

Key Words

49 retinal wave; starburst amacrine cell; retinal ganglion cell; lateral geniculate nucleus;
50 development; retinogeniculate development; afterhyperpolarization; cAMP; Ca^{2+}-activated K^+
51 channel; layer A; layer A1
52
53

54

Introduction

This article describes a neural model of how spontaneous retinal waves are formed in infant mammals, and how these waves organize activity-dependent development of a topographic map in the lateral geniculate nucleus, or LGN, with connections from each eye segregated into separate anatomical layers of the LGN (Figure 1). Recent work in imaging the retina through multi-electrode arrays [1] and fluorescent dyes [2] before eye opening in mammals, and some invertebrates, has cast new light on how these spontaneous traveling waves in the retina are formed. While their existence has been known for over two decades [3], experimentalists have just begun to untangle their molecular basis and functional implications [4-11]. Our model builds upon previous theoretical work [2, 12-14] to clarify key properties of these waves and to show how these properties may function to organize the development of the retinogeniculate map. The model includes two key cell types: starburst amacrine cells (SACs) and retinal ganglion cells (RGCs) that interact through time.
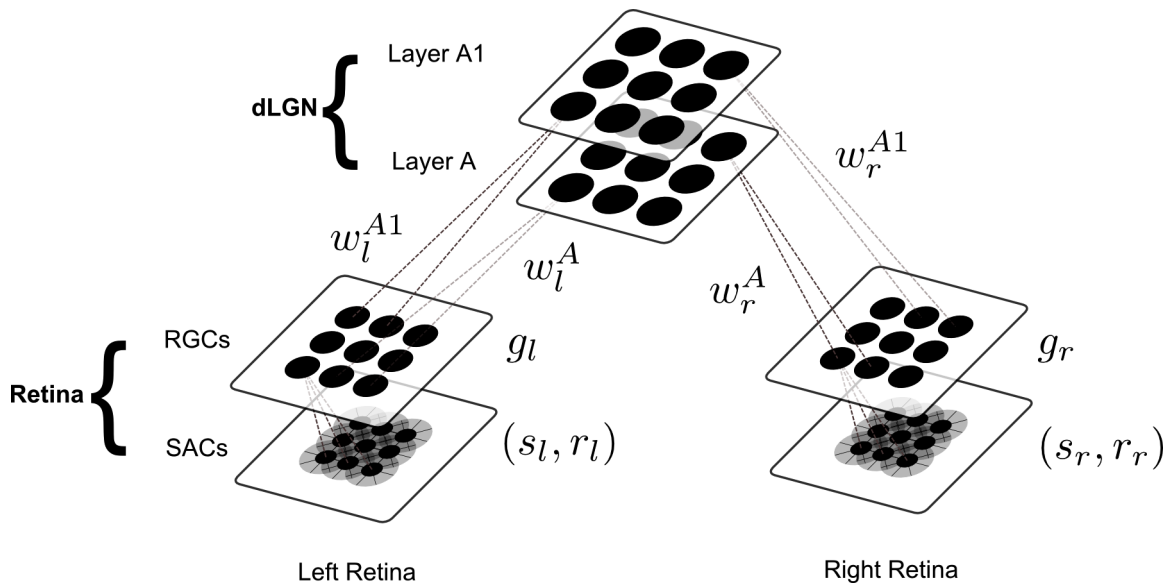

Figure 1. *A diagram of the full model circuit.*

Albeit simple, the new model goes beyond earlier modeling efforts by explicitly accounting for the role of intracellular mechanisms such as Ca^{2+}-activated K^+ channels, cAMP, and afterhyperpolarization currents (AHPs) in controlling spatiotemporal properties of retinal waves [5]. These results include novel predictions concerning how these intracellular mechanisms regulate retinal waves. For example, the model predicts that decreasing the strength of AHPs, formulated here as an activity-dependent recovery process (see equation (7)), increases the frequency and velocity of the waves generated by SACs, and vice versa for increasing the strength of AHPs. Thus, our model advances current knowledge by simulating how single-cell currents may give rise to emergent dynamical network properties, such as wave velocity, shape, and periodicity.

Retinal waves cause spontaneous bursts of action potentials in RGCs, on the order of 10-100 Hz, that move in a wave-like fashion across $1.5 - 2mm^2$ sections of the retina in the first two

83 weeks of postnatal development, just prior to eye opening in cat, ferret, and mouse. There are
84 two stages of retinal waves, normally classified into early (<P8) and late (>P8) stage waves. This
85 article concerns early stage waves only, which have been more fully characterized as spatially
86 correlated patterns of activity that travel across the RGC network. Blockade of nicotinic
87 acetylcholine receptors (nAChRs) in the retina leads to the disruption of waves, as well as of the
88 development of the early visual system [8] (although see [15]). The mature organization of the
89 mammalian LGN thus appears to be both caused [16] and maintained [17] by spontaneous retinal
90 activity. The current model simulates how the retinal waves can organize retinogeniculate map
91 development, leading to a learned map in which each eye activates a different layer (A or A1) in
92 the LGN. Moreover, retinal waves also may play a role in the early formation of receptive field
93 properties and ocular dominance columns in V1 [18].

94

95 **Materials and Methods**

96

97 *Model Retina*
98 As noted above, the model (Figure 1) incorporates interacting SACs and RGCs, in keeping with
99 experimental data [15] and the structure of previous models [2, 14] about retinal waves. Model
100 SACs occupy the first layer, where they are laterally connected to each other with isotropic
101 distance-dependent Gaussian weighting functions. Anatomical data estimate their effective input
102 radius at approximately $100\mu m$ [9]. This lateral communication approximates the function of
103 transmission via nicotinic acetylcholine receptors (nAChRs) during early development, which
104 are thought to be a critical mediator of waves and thereby retinogeniculate development [8, 19]
105 Spontaneous activity within the SACs is generated using a Poisson process.
106   All model cells are point neurons whose single compartment voltage, V_m, obeys:

107

108
$$C_m \frac{dV_m}{dt} = -(V_m - E_{\text{leak}})g_{\text{leak}} - (V_m - E_{\text{excitatory}})g_{\text{excitatory}} - (V_m - E_{\text{inhibitory}})g_{\text{inhibitory}}. \qquad (1)$$

109 In (1), C_m is the membrane capacitance; $E_{leak}, E_{excitatory},$ and $E_{inhbitory}$ are the three Nernst, or

110 reversal potentials; and g_{leak}, $g_{excitatory}$, and $g_{inhibitory}$ are the three intracellular conductances.

111 Setting $X = V_m - E_{leak}, A = g_{leak}, B = E_{excitatory} - E_{leak}, g_{Na} = g_{excitatory}, C = E_{leak} - E_{inhibitory},$ and

112 $g_K = g_{inhibitory}$, (1) becomes:

113

114
$$\frac{dX}{dt} = -AX + (B - X)g_{\text{Na}} - (C + X)g_{\text{K}}. \qquad (2)$$

115 In this notation, A is the passive decay rate, B is maximum value of potential X, and $-C$ is the
116 minimum value of X.

117

118 *Starburst Amacrine Cells*
119 The activities s_{lij} and s_{rij} of SAC cells (i, j) in the left and right eyes obey:

3

$$\frac{ds_{eij}}{dt} = -A^S s_{eij} + (B^S - s_{eij}) \left[I_{eij} + \sum_{pq} w^S_{ijpq} \left[s_{epq} \right]^+ \right] - r_{eij} \tag{3}$$

respectively. As in (2), parameter A^S in (3) is the decay rate; B^S is the excitatory saturation point; I_{lij} and I_{rij} are endogenously active inputs that are defined by a Poisson distribution:

$$\Pr\{I_{eij} = k\} = \frac{\lambda^k}{k!} e^{-\lambda}. \tag{4}$$

In (3), subscript l denotes the left eye and r the right eye. In the Poisson distribution in (4) that defines the probabilistic input term I_{eij}, Pr denotes the probability, and $\lambda = .0025$. The excitatory recurrent interactions $\sum_{pq} w^S_{ijpq} \left[s_{epq} \right]^+$ in (3) between SAC cells are mediated by Gaussian connection weights across space:

$$w^S_{ijpq} = L^S \frac{1}{2\pi\sigma^S_x \sigma^S_y} \exp\left[-\frac{(i-p)^2}{\left(\sigma^S\right)^2} - \frac{(j-q)^2}{\left(\sigma^S\right)^2} \right], \tag{5}$$

where L^S is a scaling factor, and σ^S defines the variance along the x and y axes, which are assumed to be equal, as suggested by data from imaging of SACs [9]. The recurrent signal function in (3) is a half-wave rectified function of cell activity; e.g.,

$$\left[s_{lpq} \right]^+ = \max(s_{lpq}, 0). \tag{6}$$

In (3), the inhibitory shunting term in (2) is missing, since GABAergic synapses have been shown to be excitatory in the retina during the presence of spontaneous waves [9], which could be due to changes in the intracellular concentration of chloride [20]. More precisely, if the intracellular concentration of chloride were increased until it exceeded the extracellular concentration, then chloride ions would flow out of the cell upon receptor activation via GABA.

Lastly, terms r_{lij} and r_{rij} in (3) are intracellular processes that govern each SAC cell's refractory period via afterhyperpolarization, or AHP, currents:

$$\frac{dr_{eij}}{dt} = A^R s_{eij} - B^R r_{eij}. \tag{7}$$

In (7), A^R is the rate at which each r increases, analogous to intracellular mechanisms that lead to inhibition as a result of spiking; e.g. Ca^{2+}-activated K^+ channels [21]. By the same token, B^R defines the rate with which each r decreases, thereby upregulating the excitability of each SAC, similar to the role of cAMP and its correspondent signaling cascades [5, 22]. The variable r is similar to the recovery variable used in the Fitzhugh-Nagumo equation to describe the spiking rate of a single neuron [23]. It describes the overall state of activity-dependent

148 intracellular processes that modulate a cell's firing rate. The variable r increases when the cell
149 begins to fire, and it steadily decreases once the recovery variable has sufficiently suppressed the
150 firing rate. For example, an increase in the SAC cell activity s_{lij} in (3) leads to an increase in r_{lij}
151 in (7) that, in turn, suppresses s_{lij} via (3), leading to a subsequent decrease in r_{lij} until r_{lij} can no
152 longer suppress s_{lij}. This interaction qualitatively simulates the recruitment of Ca^{2+}-activated K^+
153 channels, which have been shown to control the AHPs of SACs using *in vitro* whole cell patch
154 clamp [24]. More precisely, an increase in a cell's firing rate leads to an increase in the
155 intracellular concentration of Ca^{2+} which, in turn, opens Ca^{2+}-activated K^+ channels that act to
156 electrically shunt the cell by increasing K^+ conductance on a slow timescale, decreasing the
157 membrane resistance for tens of seconds. It also appears that these channels are voltage-
158 independent (similar to the small conductance, or SK, channels) and can only be opened by an
159 increase in cytosolic Ca^{2+} [24], although cytosolic Ca^{2+} can be affected by the conductance of
160 voltage-gated Ca^{2+} channels.
161
162 ***Retinal Ganglion Cells***
163 The SACs send half-wave rectified signals to the RGCs, which smooth SACs activity through
164 leaky integration. The activities g_{lij} and g_{rij} of RGCs in position (i, j) in the left (*l*) and right (*r*)
165 eyes obey:

$$\frac{dg_{eij}}{dt} = -A^G g_{eij} + (B^G - g_{eij})\left[\sum_{pq} w^G_{ijpq} \left[s_{epq}\right]^+\right], \tag{8}$$

167 respectively, where $e = l$ or r. In (8), the weights w^G are Gaussian functions of distance with the
168 same spatial parameters as in (5). Finally, the RGC output signals to the LGN are thresholded at
169 a positive threshold Γ^G:

$$f(g_{eij}) = \begin{cases} g_{eij} & \text{if } g_{eij} > \Gamma^G \\ 0 & \text{otherwise} \end{cases}. \tag{9}$$

171

172 By (9), model RGCs act as a set of thresholded leaky integrators that remove noise from the SAC
173 layer—that is, the RGCs only relay activity at a sufficiently high firing rate—similar to the
174 model in [2]. Supporting this assumption, experimental data have demonstrated that, outside of
175 bursting related to waves, RGC activity may not be tightly coupled to SAC activity [24]. See
176 Table 1 for the parameters for the model retina.
177

Parameter	Value	Meaning
A^S	6.5	SAC leak
B^S	5	SAC maximum excitability
σ^S	1	SAC dendritic spread
L^S	3	Weight scaling
λ	.0025	Parameter for Poisson process

A^R	8	r growth rate
B^R	.09	r decay rate
A^G	10	RGC leak
B^G	50	RGC maximum excitability
Γ^G	3	RGC output threshold
σ^G	1	RGC dendritic spread
A^L	5	dLGN leak
B^L	5	dLGN maximum excitability
α^L	11	Retinotopic bias
η	7	Noise in retinogeniculate axons
A^{RL}	1e-5	Learning rate
B^{RL}	1	growth factor

178 **Table 1.** *Parameters used for model simulations.*

179

180 ***Lateral Geniculate Nucleus Cells***

181 The RGC outputs activate cells in the dorsal LGN (dLGN) in layers A and A1 whose activities

182 x_{ij}^A and x_{ij}^{A1} at position (i, j) obey the equations:

$$\frac{dx_{ij}^A}{dt} = -A^L x_{ij}^A + (B^L - x_{ij}^A)\sum_{pqe} w_{eijpq}^A f(g_{epq}) \tag{10}$$

184 and

$$\frac{dx_{ij}^{A1}}{dt} = -A^L x_{ij}^{A1} + (B^L - x_{ij}^{A1})\sum_{pqe} w_{eijpq}^{A1} f(g_{epq}), \tag{11}$$

186 respectively. The adaptive weights w_{eijpq}^A and w_{eijpq}^{A1} in (10) and (11) from the RGC at position

187 (p,q) and eye $e = (l,r)$ to the dLGN cell at position (i, j) and layer $d = (A, A1)$ are initially

188 chosen at time 0 to obey the equations:

$$w_{eijpq}^d = \beta_e^d (\alpha_{ijpq} + N_{eijpq}^d), \tag{12}$$

190 where

$$\alpha_{ijpq} = \begin{cases} \alpha^L & \text{if } p = i \text{ and } q = j-1, j, \text{ or } j+1 \\ 0 & \text{otherwise} \end{cases} \tag{13}$$

192 and

$$N_{eijpq}^d \text{ is a random number drawn uniformly from } [0,\eta]. \tag{14}$$

194 This defines a noisy topography where arborization from retinogeniculate axons undershoots and

195 overshoots its target along the dorsoventral axis in early development [25, 26]. The eye-specific

196 bias terms β^d in (12) multiply the afferents from the left eye to layer A and the right eye to layer

197 A1 by an eye-specific scaling factor with parameter $\beta_L^A < 1$ ($\beta_R^A = 1$) for the projections from the

198 left (right) eye to layer A and $\beta_R^{A1} < 1$ ($\beta_L^{A1} = 1$) for projections from the right (left) eye to layer

199 A1. As a result, afferents from both eyes contact both layers of the LGN, albeit with a slight bias
200 to the eye that eventually dominates, prior to the critical stage of mammalian retinogeniculate
201 development of eye-specific layers [26, 27].
202   The activity-dependent release of learning-inducing neurotrophins from dLGN cells is
203 modeled by sigmoid signals of LGN activities:

$$204 \qquad X_{ij}^{A} = \frac{(x_{ij}^{A})^2}{10 + (x_{ij}^{A})^2} \qquad (15)$$

205 and

$$206 \qquad X_{ij}^{A1} = \frac{(x_{ij}^{A1})^2}{10 + (x_{ij}^{A1})^2}. \qquad (16)$$

207
208 ***Retinogeniculate Map Learning***
209 Learning in the adaptive weights w_{eijpq}^{A} and w_{eijpq}^{A1} in equations (10) and (11), from the eyes
210 $e = (L, R)$ to the LGN layers A and $, A1$ is gated on and off by these neurotrophic signals, and
211 obeys the following equations:
212

$$213 \qquad \frac{dw_{lijpq}^{A}}{dt} = A^{RL} X_{ij}^{A} \left[f(g_{lpq}) \left[B^{RL} - \sum_{pqe} w_{eijpq}^{A} \right] - w_{lijpq}^{A} \right], \qquad (17)$$

$$214 \qquad \frac{dw_{rijpq}^{A}}{dt} = A^{RL} X_{ij}^{A} \left[f(g_{rpq}) \left[B^{RL} - \sum_{pqe} w_{eijpq}^{A} \right] - w_{rijpq}^{A} \right], \qquad (18)$$

$$215 \qquad \frac{dw_{lijpq}^{A1}}{dt} = A^{RL} X_{ij}^{A1} \left[f(g_{lpq}) \left[B^{RL} - \sum_{pqe} w_{eijpq}^{A1} \right] - w_{lijpq}^{A1} \right], \qquad (19)$$

216 and

$$217 \qquad \frac{dw_{rijpq}^{A1}}{dt} = A^{RL} X_{ij}^{A1} \left[f(g_{rpq}) \left[B^{RL} - \sum_{pqe} w_{eijpq}^{A1} \right] - w_{rijpq}^{A1} \right]. \qquad (20)$$

218 Equations (17)-(20) define a self-normalizing *instar* learning law [28-30] wherein A^{RL} is a
219 learning rate and B^{RL} a limited growth factor released by coincident LGN bursting (X_{ij}^{d}), where
220 d equals A or $A1$, and RGC bursting ($f(g_{epq})$). Learning and forgetting are both gated by
221 postsynaptic activity (X_{ij}^{d}). This process could be carried out through the use of a limited
222 growth factor, such as BDNF or NT-4 [31, 32], when there is a coincident rise in the firing rates
223 of RGCs and dLGN cells [33, 34]. Competition for a limited neurotrophin is shown herein to
224 cause bounded synaptic growth. It allows for the eye with a slight initial advantage to dominate a

given layer of the dLGN. In particular, as weights with a slight bias grow, they prevent the growth of other competing weights.

Models that rely on inter-synaptic competition have used explicit divisive or subtractive normalization to achieve similar results [13, 35]. These latter approaches are not biologically realistic because it is unclear how synapses would implement global divisive normalization. The learning equations (17)-(20) can replicate map formation by using local interactions that are consistent with what is known about how synapses in the developing retinogeniculate projection compete; in particular, when a postsynaptic cell becomes active, its abutting weights can compete for growth. The parameters for the model retinogeniculate pathway are given in Table 1.
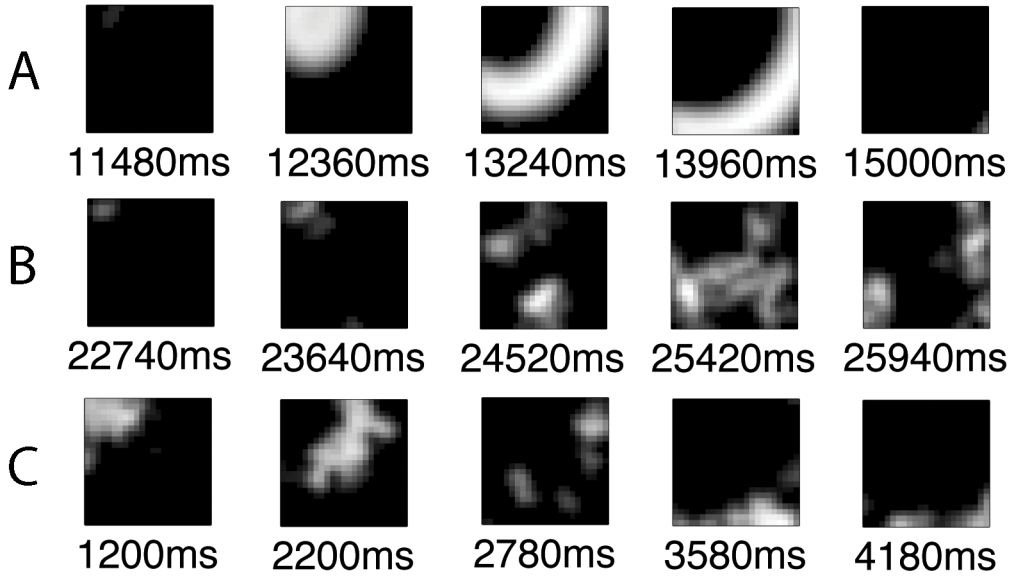
Figure 2. *Depiction of a model wave generated using the parameters given in Table 1 (A) and through randomizing SAC refractory periods (B and C). Model RGCs are shown using an intensity plot where the brightness scales with the firing rate. The waves propagate in a radially symmetric pattern due to the isotropy of the SAC lateral weights, or model dendrites. Other geometries were achieved through randomizing B^R by choosing B^R from a normal distribution centered on .09 where $\sigma = .3$ (negative values were set to zero).*

Results

Retinal Wave Simulations

Retinal waves [10] were simulated in order to tease apart the effects of excitatory and inhibitory intracellular mechanisms; e.g., the cAMP and Ca^{2+} currents that are represented in (7). These intracellular mechanisms are assumed to control the AHP of SACs that modulate wave velocity and periodicity. The model replicates the general spatiotemporal properties of waves observed *in vitro* in a number of animals, including mice and ferrets. A sample wave is depicted in Figure 2. The properties most commonly observed and quantified are the inter-wave interval (IWI), or the time between waves, and the wave velocity [1, 2, 5]. These properties were the focus of the simulations. Wave events were identified by determining if the number of active cells at a given

263 time point exceeded a predetermined threshold, similar to a method used to quantify neuronal
264 avalanches [36], which are neural events quite similar to retinal waves. The movement of the
265 center of mass (CoM) of cell activity across time was used to measure wave velocity [14], where
266 the CoM for each retina e is defined by:
267

$$CoM_e = \frac{\sum_{pq} pos_{pq} f(g_{epq})}{\sum_{pq} f(g_{epq})},$$

(21)

269 where pos_{pq} denotes position (p, q) and the RGC outputs $f(g_{epq})$ are defined in (9).
270

A

B
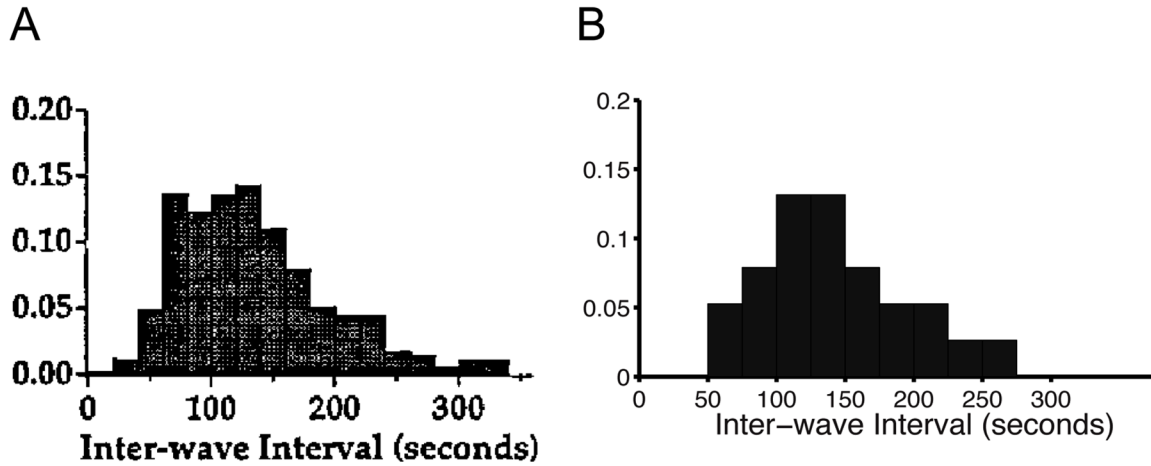
271 **Figure 3.** *Inter-wave interval (IWI) distributions from Ca^{2+}-imaging data (A) and the model*
272 *simulation (B). A comparison the IWI distributions from model simulations with Ca^{2+}-imaging*
273 *data [2]. The Ca^{2+}-imaging data is derived from multiple retinas. Likewise, the simulation*
274 *results are an aggregate of multiple simulations that used different values of A^R*
275 *(6,6.15,6.3,6.45,6.6,6.75,6.9,7.05). [Experimental data in (A) are reproduced with permission*
276 *from [2].]*
277

278 First, model simulations were compared to Ca^{2+}-imaging data from [2] that were corroborated
279 using a 512 electrode array [1]. The model was numerically integrated for 40000 seconds
280 (approximately 11 hours) using Euler's method with a time step of 20 ms, and the output of the
281 RGC layer was stored for subsequent analysis. Since the model parameters could not be directly
282 fit to biophysical data (e.g., the batch concentration of forskolin, which increases the intracellular
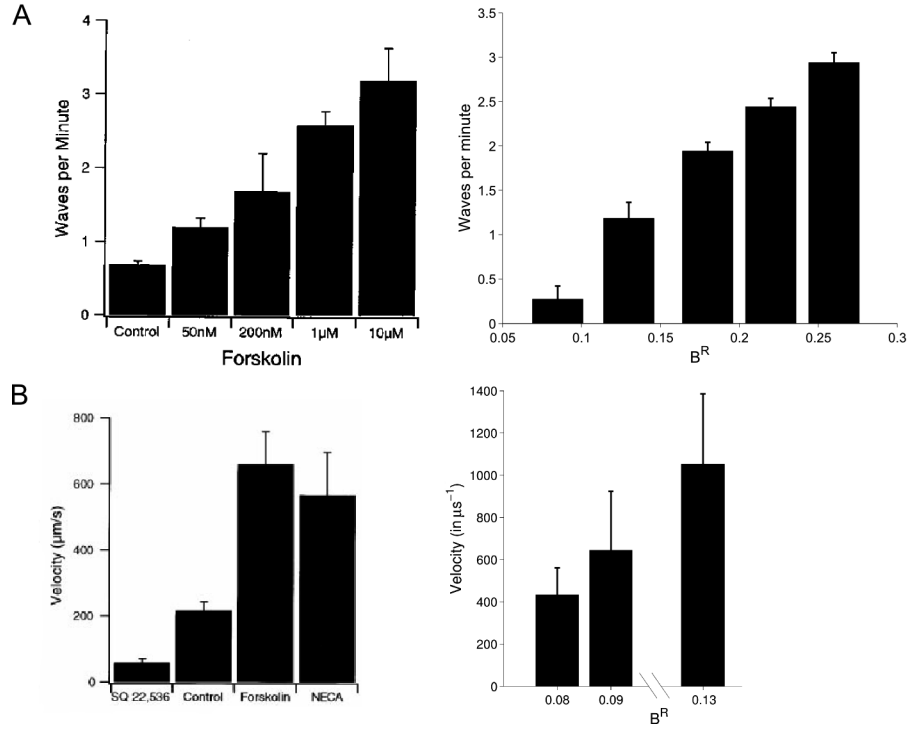283 concentration of cAMP), they were determined empirically.
284

Figure 4. *Comparison of waves per minute (A), and velocity (B), between simulations while increasing B^R in (8), a parameter analogous to excitatory intracellular mechanisms (e.g. cAMP-related signaling cascades) in experiments conducted under various levels of cAMP. In (A), the average waves per minute (WPM) is compared between the model (right) and an experiment (left) under forskolin treatment, an agonist of cAMP [5]. Here, WPM monotonically increases as a function of B^R, similar to the forskolin treatment in vitro. In (B), the average velocity is given for model simulations (right) and cAMP perturbations in the same experiment (left). Generally, velocity increases with B^R in the model, which is also observed under pharmacological manipulation of cAMP levels. For the model, the mean movement of the centroid of the wave across time is used as a measure of velocity, as in (25).*

In all the retinal simulations, waves were detected by counting the number of active cells at each time step and comparing with a pre-determined threshold. The algorithm assumes that the beginning and end of a wave are marked by crossing the threshold of 10 cells going active. Thus, if more than ten cells (out of 576) burst, a wave begins, and the wave ends as soon as less than ten cells are bursting. Each time step in between these two events is considered part of a single wave. This algorithm eased the significant computational load of analyzing the simulation results (24 x 24 values over 200000 time steps). Hundreds of identified target waves were checked by eye to ensure the validity of the algorithm.
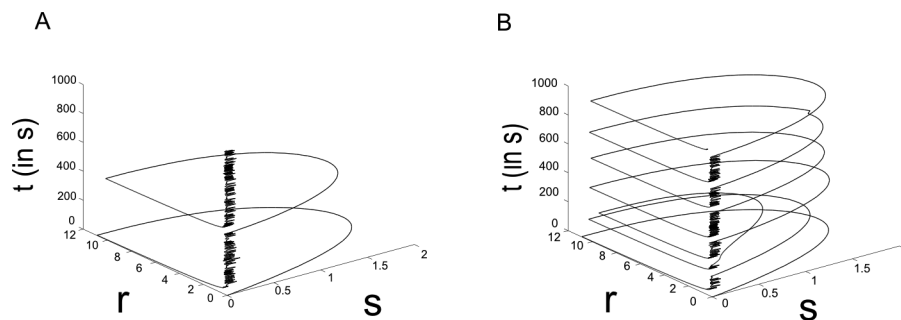
327

328

329

Figure 5. *Single cell dynamics of a model SAC when setting B^R in (8) low (A), and high (B), to .09 and .095, respectively. Shown are the dynamics of a single cell in a full simulation of the model retina over 1000 seconds. Here, s is the firing rate of the model SAC, and r the amount of inhibition due to intracellular processes. By setting B^R high, the decay rate of inhibition decreases, analogous to the application of forskolin to acute retinal slices. This has the effect of increasing both the WPM and the wave velocity (see Figure 4).*

Figure 3 shows a good qualitative match of IWI distributions between the model and experiment. Increasing parameter B^R in equation (7), analogous to increasing the level of intracellular cAMP or other intracellular excitatory mechanisms, decreases AHPs in model SACs, and thereby shifts both the IWI and velocity distributions to the right (Figure 4). Additionally, the single cell dynamics of model SACs is significantly altered; SAC cells enter an active, or bursting state (i.e., a state of sustained high firing rate) more frequently (Figure 5). Thus, model SACs control IWI, velocity, and SAC firing characteristics using activity-dependent intracellular processes.
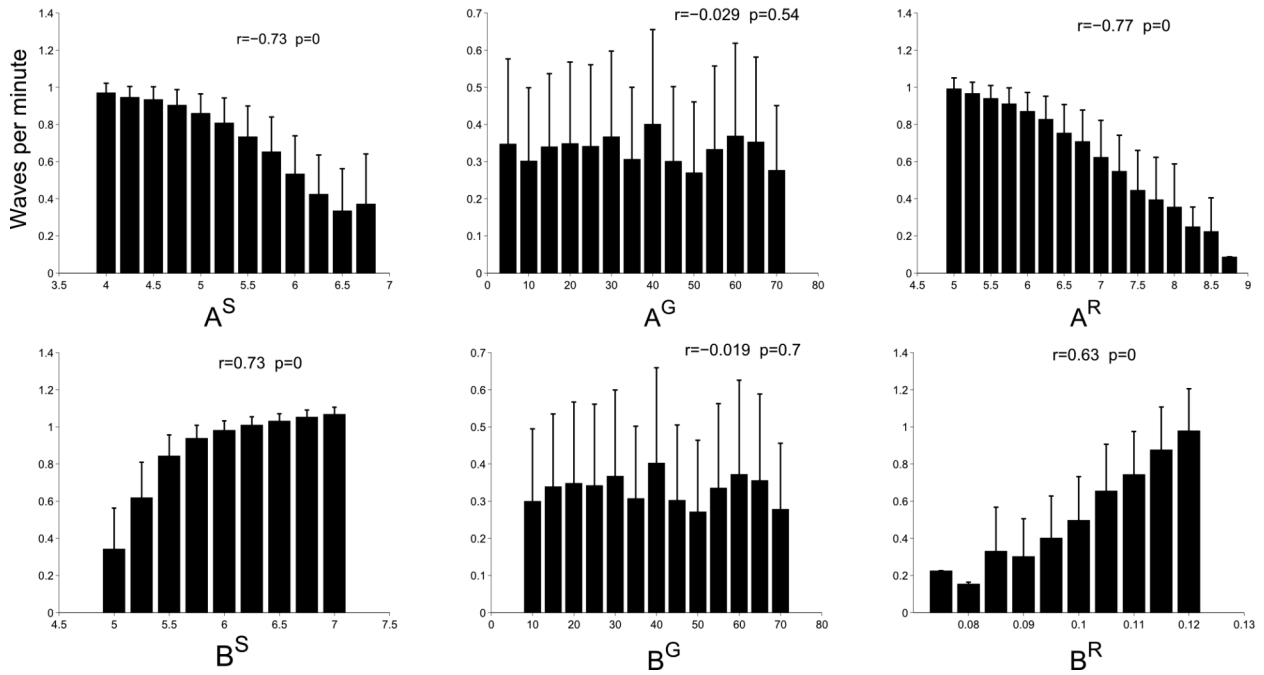
343

Figure 6. *The effect of changing model parameters on waves per minute (WPM). The effects on WPM of varying the following parameters were studied: leak A^S and maximum excitability B^S in model starburst amacrine cells (SACs)—see (3); similar parameters A^G and B^G in model retinal ganglion cells (RGCs)— see (10); and other intracellular excitatory B^R and inhibitory A^R mechanisms in the AHP currents—see (8). Increasing A^R or A^S decreases WPM, while increasing B^R or B^S increases WPM. The parameters A^G and B_G governing the behavior of model RGCs have no significant effect on WPM, indicating that SAC dynamics alter WPM.*

351 *Means of WPM across multiple simulations are shown, with error bars indicating the standard*
352 *deviation.*

353 To more comprehensively understand how model parameters affect the IWI and velocity,
354 simulations systematically explored the parameter space (see Figures 6 and 7). The results
355 demonstrate that the inhibitory and excitatory terms in the two SAC equations modulate waves in
356 complementary ways: Increasing the SAC decay rate A^S and the excitatory saturation potential
357 B^S in (3) decrease and increase waves per minute (WPM, inversely proportional to IWI) and
358 wave velocity, respectively, and similarly for A^R and B^R in (7). These results predict that
359 upregulating the decay rate or intracellular inhibitory mechanisms (e.g., cytoplasmic Ca^{2+}
360 concentration) of SACs should decrease wave velocity and WPM, while increasing maximum
361 excitability (e.g., density of voltage-gated Na^+ channels) or intracellular excitatory mechanisms
362 (e.g., intracellular cAMP concentration) should increase velocity and WPM. Additionally, these
363 simulations show a significant relationship between velocity and WPM, which has been
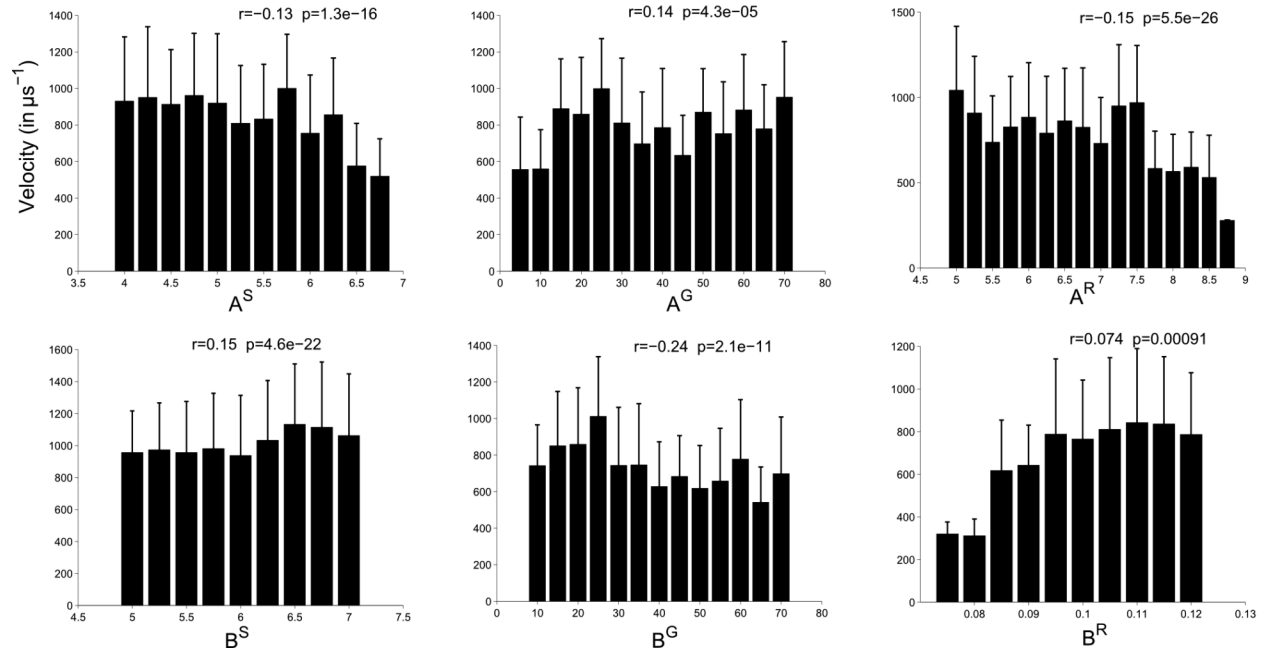364 observed in experiments [5] and other theoretical work [2].

365

366

367 **Figure 7.** *The effect of changing model parameters A^S B^S A^G B^G B^R A^R on wave velocity. The*
368 *effects on velocity are weak, but statistically significant. As with WPM, increasing A^R and*
369 *A^S decreases velocity, and vice versa for B^R and B^S. Unlike the periodicity of waves, their*
370 *velocity is significantly modulated by the properties of the model RGCs via A^G and B^G.*

371

372 Whereas all SAC parameters influence wave periodicity and velocity, the RGC parameters
373 A^G and B^G only affected wave velocity. This is due to the fast-slow dynamics present in the
374 SACs and the assumption that RGCs merely filter SAC activity en route to the dLGN.

375

Retinogeniculate Map Development Simulations

Simulations were carried out to demonstrate that waves generated within the model retina can drive the development of a retinogeniculate map whose connections from each eye are segregated into distinct LGN layers A and A1 [37, 38] (see equations (10)-(20)), Molecular guidance cues, e.g. EphA and EphB [39], presumptively form the initial topography of the retinogeniculate projection while a second stage of activity-dependent refinement prunes ectopic axonal arbors (i.e., arbors that resulted in a breakdown of retinotopy) [25, 40, 41]. The model retinogeniculate pathway focuses on this second stage of development.
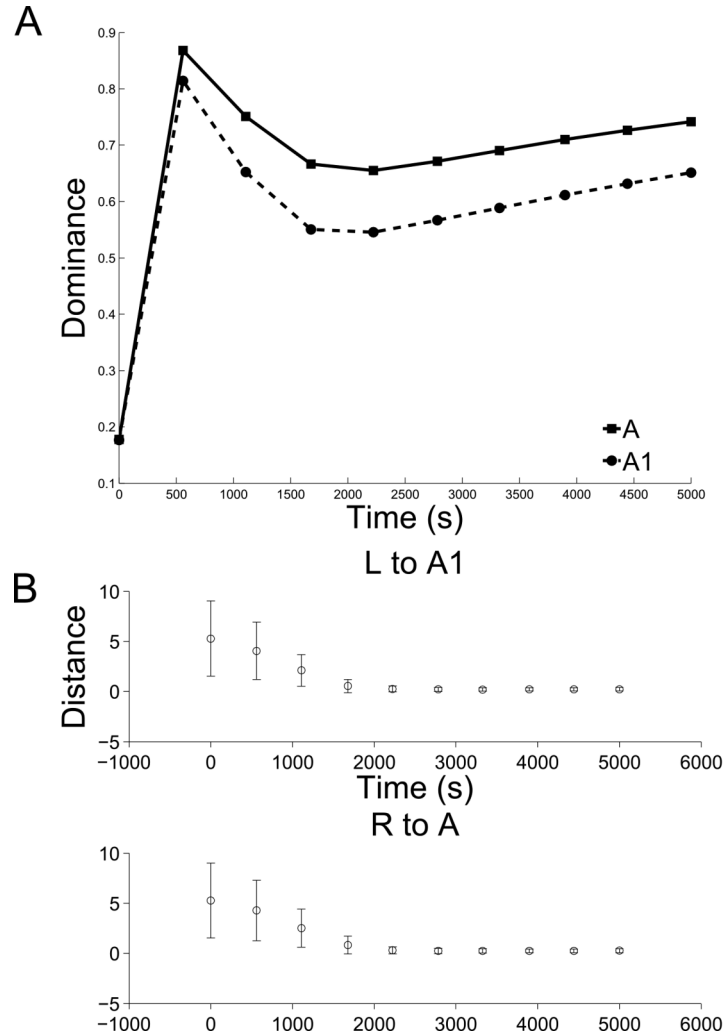

Figure 8. *Simulation of retinogeniculate development. (A) The normalized dominance of the initially biased eye grows. For both layers A and A1, the eye that is initiated with weights slighter larger than the other comes to `dominate' that layer over the course of 5,000s of waves (see (22)). (B) Additionally, the mean distance of the CoM from an ideal CoM for the retinogeniculate weights decreases, indicating that the weights projecting to each dLGN cell become increasingly refined; in particular, ectopic projections are pruned away.*

394 The simulations demonstrate that retinal waves can drive the development of eye-specificity in
395 dLGN layers (Figure 8) as well as refinement of dLGN topography in a single hemisphere
396 (Figure 9). To measure eye-specificity, a normalized measure of the difference in total
397 magnitude (DOM) between the weights projecting from each eye is used:
398

$$DOM_A = \frac{\sum\limits_{ijpq} w^A_{rijpq} - \sum\limits_{ijpq} w^A_{lijpq}}{\sum\limits_{ijpqe} w^A_{eijpq}}$$

399   (22)

$$DOM_{A1} = \frac{\sum\limits_{ijpq} w^{A1}_{lijpq} - \sum\limits_{ijpq} w^{A1}_{rijpq}}{\sum\limits_{ijpqe} w^{A1}_{eijpq}}$$

400   Then, topography was assayed as the summed Euclidean distance between the center-of-mass
401 (CoM) of the weights from the RGC at position (p,q) and projecting to all dLGN cells (i,j) in
402 layers A and A1, respectively:

$$CoM^A_{epq} = \frac{\sum\limits_{ij} pos_{ij} w^A_{eijpq}}{\sum\limits_{ij} w^A_{eijpq}}$$

403   (23)

$$CoM^{A1}_{epq} = \frac{\sum\limits_{ij} pos_{ij} w^{A1}_{eijpq}}{\sum\limits_{ij} w^{A1}_{eijpq}}$$

404 and its correct retinotopic position (i = p, j = q) (see Figure 9B).
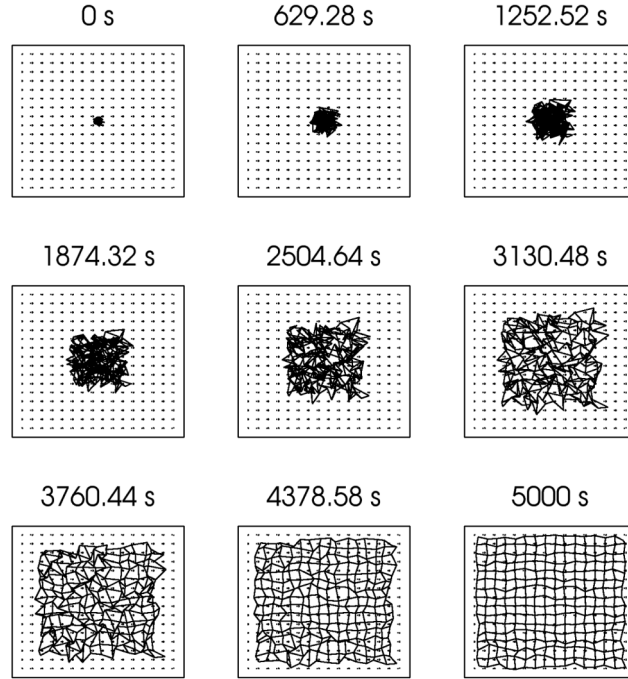405
406

14

Figure 9. *Change in CoM for the model retinogeniculate pathway (from the left retina to layer A1 of the dLGN, both layers develop simultaneously but all results are shown in one pathway for convenience). Using the method of visualizing retinogeniculate weights from [34], the CoM of the weights projecting to a given dLGN cell (see (23)) is depicted as a node connected to its 4 nearest neighbors in solid black (2 for cells at the edge, since the boundaries are non-periodic). The ideal topography is visualized by the dotted grid defined by the points in a_{ijpq}, where $p = i$ and $q = j$ (site of initial retinotopic bias). Over the course of the simulation, the CoMs approach the ideal (the time during the simulation at which the CoMs were assessed is shown just above each figure).*

First, development of the retinogeniculate pathway was simulated for 5,000 seconds (simulated time) using the standard parameters to generate retinal waves (see Table 1), and each wave was distributed between the retinas such that only one retina was active at a time and consecutive waves occurred in different retinas. Under these conditions, the retinas that were slightly biased to project to each dLGN layer (left retina to dLGN layer A1 and the right retina to dLGN layer A) quickly dominated the retinogeniculate projections at the expense of the opposite retina, indicated by the sharp rise in DOM for layers A and A1 in the first 500 seconds of the simulation (see Figure 8). At the same time, yet on a much slower timescale, the topography of the dLGN was refined (see Figure 9). Thus, the learning rule used in the model retinogeniculate pathway accounts for the development of both layer-specificity and a refined topography.

Waves were also generated using different sets of parameters to simulate perturbations to the retina and their effect on retinogeniculate development. First, B^R (see (7)) was increased from .12 to .2 to generate faster waves with smaller inter-wave interval distributions (see Figures 3 and 4). This sped up the formation of layer-specificity and, more dramatically, the topography

15

refinement proportional to the increase in B^R (see Figure 10). When $B^R = .2$, the topography refinement is sped up dramatically, with a noticeable increase in the speed of the initial rise in DOM for both layers. These parameter settings are analogous to the use of forskolin to accelerate waves *in vitro* [5].
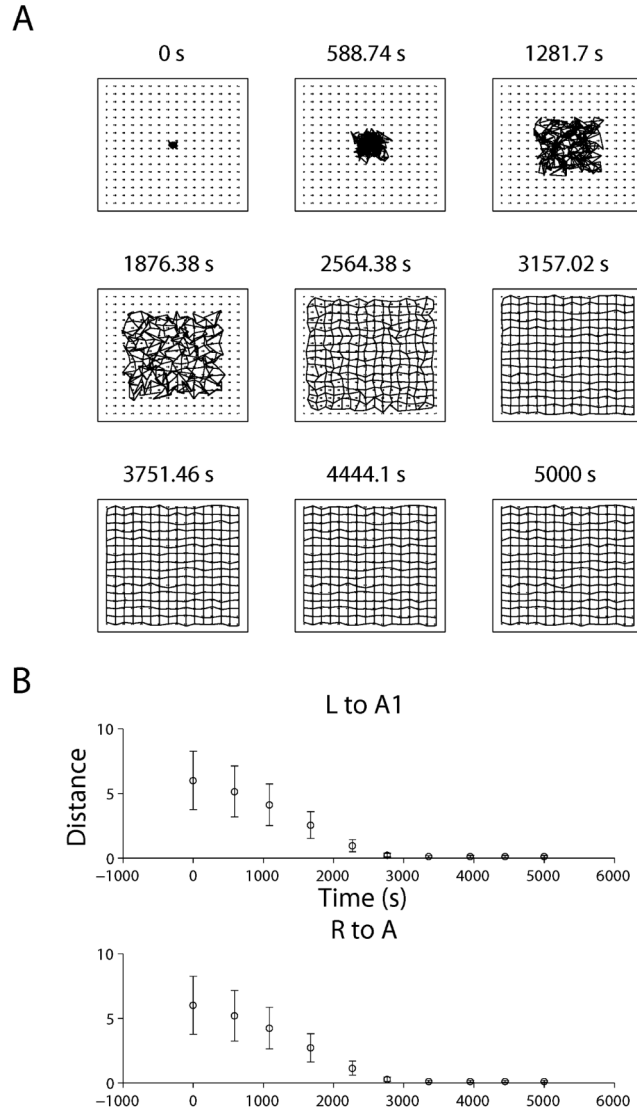

Figure 10. *Retinogeniculate development accelerates as wave velocity and wave frequency increases by increasing B^R (see Figure 4). (A) The CoMs approach the ideal grid at a faster pace with accelerated waves, also shown by the sharper decrease in the mean distance of the CoM from their targets (B).*

Next, to divorce layer-specificity from topography refinement, 'random' waves were generated by replacing the activity of RGCs with Poisson noise ($\lambda = .5$), and then interleaving the noise between the two retinas, where each retina was active for one second with the other completely inactive. Intuitively, this would cause the biased retinas to dominate the appropriate layers in the

477   dLGN since the two eyes were still anti-correlated, yet the topography would not be refined due
478   to the lack of spatially local input. Indeed, this is what happened in the model, as DOM
479   increased similar to the other simulations, yet the CoM for each dLGN cell did not approach its
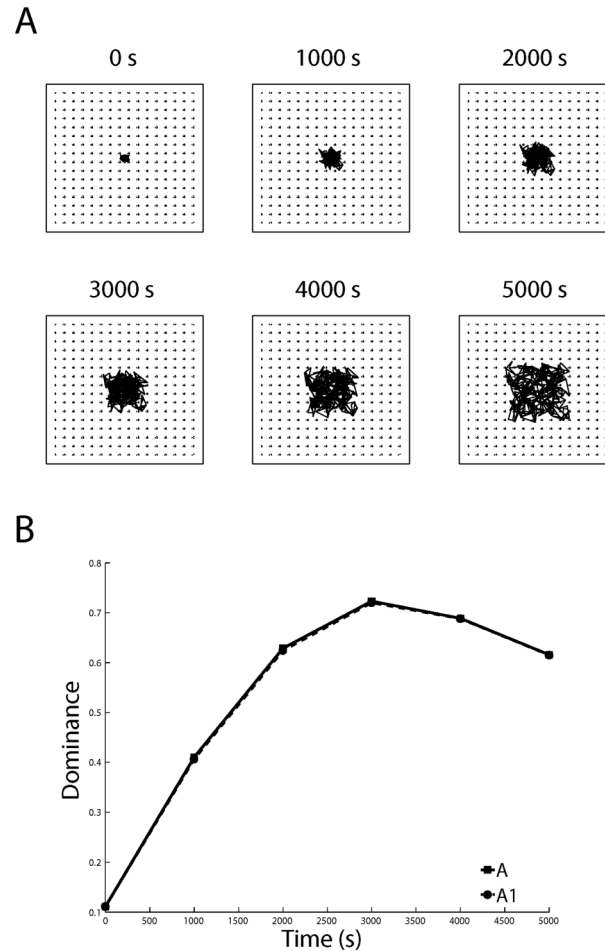480   ideal position on the grid (Figure 11).

481
482
483
484
485
486
487
488
489
490
491
492
493
494
495
496
497
498
499
500
501
502
503
504
505
506
507
508
509
510

511 ***Figure 11.*** *A proper topography fails to develop in the absence of structured retinal input. In*
512 *these simulations, the dLGN received interleaved Poisson noise from each eye instead of retinal*
513 *waves (thus preserving the anti-correlated activity between retinas). (A) The CoMs do not*
514 *approach the grid as in Figures 9 and 10 (normal and accelerated waves), yet (B) the proper*
515 *eye-specificity develops.*

516   Finally, waves of different geometries were simulated by randomizing the afterhyperpolarization
517   period of the SACs by setting B^R for each cell to values drawn from a Gaussian distribution
518   centered at .09 with σ set to .15, .2 and .3 (example waves are shown in Figure 2), with negative
519   values set to zero. A small amount of variability $\sigma = .15$ had a minimal effect on

520 retinogeniculate development, while setting $\sigma = \{.2, .3\}$ prevented full refinement of the dLGN
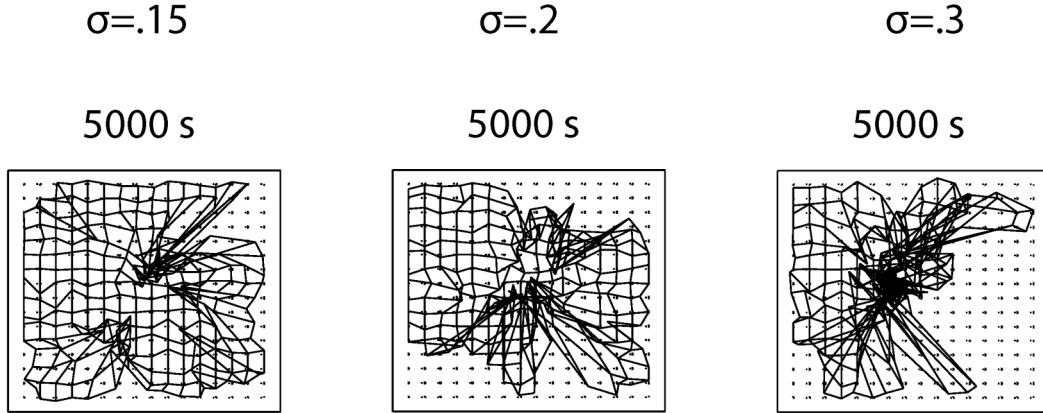521 topography, with the CoMs forming a "crumpled" pattern (Figure 12).
522

523
524 ***Figure 12.*** *The retinogeniculate pathway still develops in the presence of waves generated by*
525 *SACs with randomized refractory periods. The shape of retinal waves was altered by*
526 *randomizing B^R (see Figure 2), by drawing B^R from a normal distribution centered at .09 with*
527 *σ set to .15, .2 and .3 (negative values were set to 0). The final state of the model*
528 *retinogeniculate projection in each case is shown. Clearly, the width of the distribution affects*
529 *retinogeniculate development, with the CoMs for many dLGN cells do not fully reach their*
530 *targets on the ideal grid.*
531

Discussion

533 Tables 2 and 3 compare the proposed model with previous models. One innovation of the retinal
534 dynamics in the current model is the use of a recovery variable, *r*, as in (7), to approximate the
535 dynamics of Ca^{2+}-activated and CAMP-sensitive K^+ channels. Godfrey and Swindale [14]
536 described a simpler model that utilizes an activity-dependent refractory period. Their model
537 employs a countdown mechanism whereby a cell necessarily spikes after a variable decays to
538 zero. This hypothesis does not help to explain mechanistically how the intracellular processes
539 that underlie SAC AHPs govern wave dynamics. Another recent model of retinal waves from
540 Hennig et al. [42] uses the idea that SACs are governed by intrinsic cellular noise and slower
541 activity-dependent Ca^{2+} processes that dictate afterhyperpolarization periods. This is more
542 similar to our model and is quite biophysically realistic. Our approach captures most of the
543 dynamics present in this spiking model, yet is significantly simpler and is more amenable to
544 embedding in a larger model of retinogeniculate development, which is not simulated by Hennig
545 et al. More precisely, in our model, the recovery variable *r* simulates lumped intracellular
546 inhibitory mechanisms, based on whole-cell patch clamp [24] and Ca^{2+}-imaging [5] data.

18

547 Similar to the role of the recovery variable in the Fitzhugh-Nagumo model of a spiking neuron, r
548 suppresses the firing rate of SACs after a prolonged period of heightened firing. This
549 approximates the process of slow Ca^{2+} accumulation in the cytosol during bursting, which
550 progressively opens K^+ channels that electrically shunt a given SAC. As the channels are slow
551 to close, the SAC remains hyperpolarized or refractory for tens of seconds during the AHP,
552 which regulates the periodicity of retinal waves observed *in vitro.* Additionally, upregulating
553 cAMP through either uncaging techniques or bath application of forskolin reduces AHPs [5, 24],
554 an effect simulated by the model (see Figure 4). Thus, the pacemaking mechanism of the model
555 retina is cell-autonomous since it is regulated by intracellular processes and is effected by both
556 Ca^{2+} and cAMP, which agrees with whole-cell patch clamp data [24] wherein SACs rhythmically
557 depolarized even after the complete blockage of synaptic transmission.

558

Reference	Dynamical retina	Activity-dependent refractoriness	Retinogeniculate simulation
Haith, 1995			√
Eglen, 1999			√
Elliot and Shadbolt, 1999	√		√
Feller et al., 1997	√		
Godfrey and Swindale, 2007	√	√	
Hennig et al., 2009	√	√	
Proposed model	√	√	√

559 ***Table 2.*** *Comparision of retinogeniculate models.*

560

Reference	Dynamical dLGN cell simulation	Competition for neurotrophin
Haith, 1995	√	
Eglen, 1999	√	

Elliot and Shadbolt, 1999		√
Proposed model	√	√

Table 3. *Comparison of models that simulate the dLGN.*

This foundation enables our simulation of retinogeniculate development to use a biologically plausible dynamical system with activity-dependent refractoriness to generate retinal waves. Some models simply move the center of pre-computed distributions (e.g., a Gaussian) to approximate the bump of activity that sweeps across the retinal sheet during waves [13, 35], while others use a pre-determined refractory period that is not governed by a dynamical process [2, 34] (e.g., their model SACs are forced to not fire for a given interval after bursting). Our model also demonstrates how a simple, but biologically realistic post-synaptically gated learning rule [28] based on competition for a growth factor, as in equations (17)-(20), can simultaneously lead to eye-specificity and to the refinement of the retinogeniculate projection. That is to say, the model waves lead to LGN activity, which, in turn, induces learning where the correlations between LGN and RGC activity are the strongest. This competition obviates the need for a biologically unrealistic explicit divisive normalization term such as is used in [13, 34, 35].

In summary, the proposed model builds on and goes beyond previous work by being the first to include both: (1) a fully dynamical explanation and simulation of retinal waves that clarifies the functional role of intracellular AHP currents, and (2) a learning rule that exploits competition for a limited neurotrophin to induce topography refinement and the dominance of one eye over the other in each dLGN layer. Testing the model's predictions can provide additional experimental data with which to develop future model refinements (see Table 3).

References

1. Stafford BK, Sher A, Litke AM, Feldheim DA (2009) Spatial-temporal patterns of retinal waves underlying activity-dependent refinement of retinofugal projections. Neuron 64: 200–212.
2. Feller MB, Butts DA, Aaron HL, Rokhsar DS, Shatz CJ (1997) Dynamic processes shape spatiotemporal properties of retinal waves. Neuron 19: 293–306.
3. Meister M, Wong RO, Baylor DA, Shatz CJ (1991) Synchronous bursts of action potentials in ganglion cells of the developing mammalian retina. Science (New York, NY) 252: 939–943.
4. Feller MB, Wellis DP, Stellwagen D, Werblin FS, Shatz CJ (1996) Requirement for cholinergic synaptic transmission in the propagation of spontaneous retinal waves. Science (New York, NY) 272: 1182–1187.
5. Stellwagen D, Shatz CJ, Feller MB (1999) Dynamics of retinal waves are controlled by cyclic amp. Neuron 24: 673–685.
6. Sernagor E, Eglen SJ, O'Donovan MJ (2000) Differential effects of acetylcholine and glutamate blockade on the spatiotemporal dynamics of retinal waves. Journal of Neuroscience 20: 56RC+.
7. Zhou ZJ (2001) The function of the cholinergic system in the developing mammalian retina. Progress in Brain Research 131: 599–613.
8. Feller MB (2002) The role of nachr-mediated spontaneous retinal activity in visual system development. Journal of Neurobiology 53: 556–567.
9. Zheng Jj, Lee S, Zhou (2004) A developmental switch in the excitability and function of the starburst network in the mammalian retina. Neuron 44: 851–864.
10. Firth S, Wang C, Feller M (2005) Retinal waves: mechanisms and function in visual system development. Cell Calcium 37: 425–432.
11. Blankenship AG, Ford KJ, Johnson J, Seal RP, Edwards RH, et al. (2009) Synaptic and extrasynaptic factors governing glutamatergic retinal waves. Neuron 62: 230–241.
12. Burgi PY, Grzywacz NM (1994) Model for the pharmacological basis of spontaneous synchronous activity in developing retinas. Journal of Neuroscience 14: 7426–7439.
13. Eglen SJ (1999) The role of retinal waves and synaptic normalization in retinogeniculate development. Philosophical transactions of the Royal Society of London Series B, Biological sciences 354: 497–506.
14. Godfrey KB, Swindale NV (2007) Retinal wave behavior through activity-dependent refractory periods. PLoS Comput Biol 3: e245+.
15. Sun C, Warland DK, Ballesteros JM, van der List D, Chalupa LM (2008) Retinal waves in mice lacking the β2 subunit of the nicotinic acetylcholine receptor. Proceedings of the National Academy of Sciences of the United States of America 105: 13638–13643.
16. Torborg C, Feller M (2005) Spontaneous patterned retinal activity and the refinement of retinal projections. Progress in Neurobiology 76: 213–235.
17. Chapman B (2000) Necessity for afferent activity to maintain eye-specific segregation in ferret lateral geniculate nucleus. Science 287: 2479–2482.
18. Huberman AD, Speer CM, Chapman B (2006) Spontaneous retinal activity mediates development of ocular dominance columns and binocular receptive fields in v1. Neuron 52: 247–254.

19.   Bansal A, Singer JH, Hwang BJ, Xu W, Beaudet A, et al. (2000) Mice lacking specific nicotinic acetylcholine receptor subunits exhibit dramatically altered spontaneous activity patterns and reveal a limited role for retinal waves in forming on and off circuits in the inner retina. Journal of Neuroscience 20: 7672–7681.

20.   Cherubini E, Gaiarsa J, Ben-Ari Y (1991) GABA: an excitatory transmitter in early postnatal life. Trends in Neurosciences 14: 515–519.

21.   Sah P (2002) Channels underlying neuronal calcium-activated potassium currents. Progress in Neurobiology 66: 345–353.

22.   Dunn T, Wang C, Colicos M, Zaccolo M, DiPilato L, et al. (2006) Imaging of cAMP levels and protein kinase A activity reveals that retinal waves drive oscillations in second-messenger cascades. Journal of Neuroscience 26: 12807.

23.   Fitzhugh R (1961) Impulses and physiological states in theoretical models of nerve membrane. Biophysical Journal 1: 445–466.

24.   Zheng J, Lee S, Zhou ZJ (2006) A transient network of intrinsically bursting starburst cells underlies the generation of retinal waves. Nature Neuroscience 9: 363–371.

25.   Udin SB, Fawcett JW (1988) Formation of topographic maps. Annual Review of Neuroscience 11: 289–327.

26.   Sretavan DW, Shatz CJ (1987) Axon trajectories and pattern of terminal arborization during the prenatal development of the cat's retinogeniculate pathway. Journal of Comparative Neurology 255: 386–400.

27.   Shatz CJ (1983) The prenatal development of the cat's retinogeniculate pathway. Journal of Neuroscience 3: 482–499.

28.   Grossberg S, Seitz A (2003) Laminar development of receptive fields, maps and columns in visual cortex: the coordinating role of the subplate. Cerebral Cortex 13: 852–863.

29.   Grossberg S, Williamson JR (2001) A neural model of how horizontal and interlaminar connections of visual cortex develop into adult circuits that carry out perceptual grouping and learning. Cerebral Cortex 11: 37–58.

30.   Grossberg S, Williamson JR (1999) A self-organizing neural system for learning to recognize textured scenes. Vision Research 39: 1385–1406.

31.   Riddle DR, Lo DC, Katz LC (1995) Nt-4-mediated rescue of lateral geniculate neurons from effects of monocular deprivation. Nature 378: 189–191.

32.   Bonhoeffer T (1996) Neurotrophins and activity-dependent development of the neocortex. Current Opinion in Neurobiology 6: 119–126.

33.   Mcallister KA, Katz LC, Lo DC (1996) Neurotrophin regulation of cortical dendritic growth requires activity. Neuron 17: 1057–1064.

34.   Elliott T, Shadbolt NR (1999) A neurotrophic model of the development of the retinogeniculocortical pathway induced by spontaneous retinal waves. Journal of Neuroscience 19: 7951–7970.

35.   Haith GL (1998) Modeling activity-dependent development in the retinogeniculate projection. Ph.D. thesis, Stanford, CA, USA. http://portal.acm.org/citation.cfm?id=927417.

36.   Beggs JM, Plenz D (2003) Neuronal avalanches in neocortical circuits. Journal of Neuroscience 23: 11167–11177.

37.   Huberman AD, Wang GY, Liets LC, Collins OA, Chapman B, et al. (2003) Eye-specific retinogeniculate segregation independent of normal neuronal activity. Science 300: 994–998.

673   38.   Huberman A (2007) Mechanisms of eye-specific visual circuit development. Current
674   Opinion in Neurobiology 17: 73–80.

675   39.   Oleary D, Mclaughlin T (2005) Mechanisms of retinotopic map development: Ephs,
676   ephrins, and spontaneous correlated retinal activity, Molecular Neurobiology Laboratory, The
677   Salk Institute, 10010 North Torrey Pines Road, La Jolla, CA 92037, USA. doleary@salk.edu,
678   volume 147 of *Progress in Brain Research*. pp. 43–65. doi: 10.1016/S0079-6123(04)47005-8.
679   http://dx.doi.org/10.1016/S0079-6123(04)47005-8.

680   40.   Sretavan DW, Shatz CJ, Stryker MP (1988) Modification of retinal ganglion cell axon
681   morphology by prenatal infusion of tetrodotoxin. Nature 336: 468–471.

682   41.   Wong ROL (1999) Retinal waves and visual system development. Annual Review of
683   Neuroscience 22: 29–47.

684   42.   Hennig M, Adams C, Willshaw D, Sernagor E (2009) Early-stage waves in the retinal
685   network emerge close to a critical state transition between local and global functional
686   connectivity. The Journal of Neuroscience 29: 1077.

687